A nonlocal model of dissociative electron attachment and vibrational excitation of NO

C. S. Trevisan,[1] K. Houfek,[2] Z. Zhang,[2] A. E. Orel,[1] C. W. McCurdy,[2,3] and T. N. Rescigno[2]

[1]*Department of Applied Science, University of California, Davis, CA 95616*
[2]*Chemical Sciences, Lawrence Berkeley National Laboratory, Berkeley, CA 94720**
[3]*Department of Applied Science and Department of Chemistry, University of California, Davis, CA 95616*

(Dated: March 17, 2005)

We present the results of a study of elastic scattering and vibrational excitation of NO by electron impact in the low-energy (0-2 eV) region where the cross sections are dominated by resonance contributions. The $^3\Sigma^-$, $^1\Delta$ and $^1\Sigma^+$ NO^- resonance lifetimes are taken from our earlier study [Phys. Rev. A **69**, 062711 (2004)], but the resonance energies used here are obtained from new configuration-interaction studies. Here we employ a more elaborate nonlocal treatment of the nuclear dynamics, which is found to remedy the principal deficiencies of the local complex potential model we employed in our earlier study, and gives cross sections in better agreement with the most recent experiments. We also present cross sections for dissociative electron attachment to NO leading to ground state products, $O^-(^2P) + N(^4S)$. The calculations show that, while the peak cross sections starting from NO in its ground vibrational state are very small ($\sim 10^{-20}$cm^2), the cross sections are extremely sensitive to vibrational excitation of the target and should be readily observable for target NO molecules excited to $\nu = 10$ and above.

PACS numbers: 34.80.Gs

I. INTRODUCTION

Low-energy electron interactions with nitric oxide are of interest in a broad range of chemical, physical and atmospheric processes. NO is also used as a plasma gas and plays important functional roles in a variety of physiological systems. Although there have been a number of experimental studies on the low-energy behavior of the electron-NO collision cross sections [1–9], relatively little has been done on the theoretical front [10, 11], particularly in the energy region below 2 eV, which is dominated by negative ion resonances. Calculations in this energy range were initiated in our previous study (Zhang *et al.* [12]), which presented *ab initio* determinations of elastic and vibrational excitation cross sections using the local complex potential or "boomerang" model, with resonance parameters extracted from electronic fixed-nuclei variational scattering calculations. While those calculations were successful in capturing the essential features of the measured cross sections and confirmed the interpretation that the prominent features in the elastic and vibrational excitation cross sections arise from $^3\Sigma^-$ and $^1\Delta$ negative ion states, they also revealed deficiencies in the local complex potential model, most notably in the threshold behavior of the cross sections, that arise when the transiently excited vibrational levels of the anion are energetically close to the vibrational levels of the neutral target.

In our previous study [12] we speculated that nonlocal effects – beyond the boomerang model – would be needed to achieve quantitative agreement with measured cross sections, particularly for the first peaks in the cross sections for excitation of higher vibrationally excited states. New experimental determinations of the cross sections by Allan [9, 13] have since appeared, which differ near threshold from the experiments [5, 7, 8] with which we originally compared. The new measurements do not show the dramatic suppression of peaks near threshold that some earlier experiments suggested. These facts prompted the present study, in which the nuclear dynamics problem is treated with a more elaborate nonlocal resonance model that should be better able to treat the threshold region.

The present study also includes the calculation, using the same nonlocal model, of dissociative electron attachment (DA) cross sections, from both ground and vibrationally excited target states, that proceed through the $^3\Sigma^-$ anion state and produce ground state fragments. Near-threshold DA to NO has been studied for several decades (see Brunt and Kieffer [14], Krishnakumar and Srivastava [15] and references therein) and, in principle, can proceed via the following three channels:

$$e + NO \rightarrow O^-(^2P) + N(^4S) \quad (1)$$

$$e + NO \rightarrow O^-(^2P) + N^*(^2D) \quad (2)$$

$$e + NO \rightarrow O^-(^2P) + N^*(^2P) \quad (3)$$

Although several experimental studies have observed DA associated with channels (2) and (3), detection of DA channel (1) has been controversial. Orient and Chutjian [16] claimed to have measured ground state fragments of reaction channel $e + NO \rightarrow O^-(^2P) + N(^4S)$, reporting it as the most abundant channel in the DA to

*Permanent address: Institute of Theoretical Physics, Faculty of Mathematics and Physics, Charles University Prague, V Holešovičkách 2, 180 00 Praha 8, Czech Republic

NO. However, several studies performed afterward [17–20] found no indication of the occurrence of ground-state fragments in their measurements, consistently reporting (2) as the major DA channel, with reaction channel (3) making a smaller contribution. Our calculations show that, although cross sections that proceed through reaction channel (1) are negligibly small when DA proceeds from the vibrational ground state of NO, significantly enhanced cross sections are obtained when the target is vibrationally excited.

The fixed-nuclei R-dependent energies and widths of the various negative ion states form the basis for a study of the nuclear dynamics. Our present study uses the resonance widths of Zhang *et al.* [12], which were in turn obtained from the results of fixed-nuclei complex Kohn variational scattering calculations. The calculated cross sections are found to be extremely sensitive to the relative positions of the neutral and negative ion states. We have therefore carried out large-scale configuration interaction (CI) calculations in an attempt to better position the neutral NO and the $^3\Sigma^-$, $^1\Delta$ and $^1\Sigma^+$ anion states. These new CI curves lie closer to the semi-empirical curves obtained by Teillet-Billy and F. Fiquet-Fayard [21] and provide a more accurate description of the low-lying excited states of NO^- than the coupled-cluster (CC) potential curves employed in the previous study of Zhang *et al.*

Using these new potentials we have computed elastic and vibrationally inelastic cross sections to compare the results from the local complex potential (or "boomerang") model, the local complex potential model modified by the introduction of "barrier penetration factors," and a nonlocal model described below. The nonlocal model was used in our final calculations of vibrational excitation and dissociative attachment. As will be shown below, the present results obtained with more accurate resonance curves and the nonlocal model represent a considerable improvement over the boomerang model used in our previous calculations and are in reasonably good agreement with the most recent experimental measurements.

The theoretical formulation we have used is described in the following section. Section III presents the computational details of the present theoretical study together with our results and, where possible, comparisons to both the previous local complex potential model and recent experimental data. We conclude with a brief discussion.

II. THEORETICAL FORMULATION AND IMPLEMENTATION

As explained by Zhang *et al.* [12], a simple molecular orbital picture suffices to explain the general features of low-energy electron-NO scattering. The ground state of NO has $^2\Pi$ symmetry, corresponding to a single 2π electron outside a closed-shell core. By adding a second 2π electron, one can form negative ion states with symmetries $^3\Sigma^-$, $^1\Delta$ or $^1\Sigma^+$, which, by analogy with O_2, are expected to be separated by only a few electron volts. Fixed-nuclei electron-NO scattering calculations in these overall symmetries, at low energies, produce amplitudes (T-matrices) that display prominent resonant behavior that depends strongly on the internuclear separation. The low-energy (0-2 eV) electron-NO elastic and vibrationally inelastic cross sections are found to be dominated by contributions from these negative ion resonances. To explain the rich structure observed in the various cross sections, one needs an accurate characterization of the $R-$dependent resonance energies and lifetimes as well as a suitable model for calculating the nuclear dynamics.

The nonlocal formulation we employ here, as well as the local complex potential approach used previously by Zhang *et al.*, reveal an important property of these collisions, and that is that the contributions of the three resonances to the cross section are independent. Since the resonances belong to different total symmetries, their contributions to the observed cross sections are strictly additive; the resonances may overlap but they do not interfere. Thus, the nonlocal potential calculations can be carried out separately for each resonance and these results can be combined to produce the physically observed cross sections.

A. Local and nonlocal potential models

Local complex potential — We begin with a description of the local complex potential or "boomerang" approach to resonant collisions. The theory, which is formulated entirely within the Born-Oppenheimer approximation, has been derived in several ways [22–24] to arrive at a nuclear wave equation that governs the nuclear dynamics associated with the resonance state.

The nuclear wave equation at total energy E is

$$(E - K_R - V_{res})\xi_\nu = \phi_\nu \tag{4}$$

where K_R is the nuclear kinetic energy operator, V_{res} is the anion potential,

$$V_{res}(R) = E_{res}(R) - i\Gamma(R)/2 \tag{5}$$

and ξ_ν is the nuclear wave function associated with the electronic resonance state. The position and width of the resonance that form the anion potential are E_{res} and Γ respectively.

The driving term for the nuclear wave equation, or "entry amplitude", ϕ_ν is defined as

$$\phi_\nu(R) = \left(\frac{\Gamma(R)}{2\pi}\right)^{1/2} \eta_\nu(R), \tag{6}$$

where η_ν is the initial vibrational wave function of the neutral target.

The local complex potential model is expressed in Eqs. (4-6) in its original or "boomerang" form, and provides

the wave function ξ_ν from which the cross sections can be calculated as described below.

Barrier penetration factor –In general, cross sections computed with the entry amplitude in Eq. (6) will not have the correct energy dependence near threshold and will thus be inaccurate at very low scattering energies [25, 26]. This problem was addressed in the second model we consider here which is a modification of the local complex potential model with a "barrier penetration factor" [27, 28]. This modification involves the introduction of an *ad hoc* function of the electron momentum k into the entry and exit amplitudes.

This idea is based on identifying the angular momentum, l, that corresponds to the lowest partial wave that contributes to the resonance and enforcing a threshold law corresponding to that value of l. We define the quantity γ as:

$$\gamma(k,R) = \begin{cases} k/k(R) & \text{if } k < k(R) \\ 1 & \text{otherwise} \end{cases} \tag{7}$$

where k is the physical electron momentum, and $k(R)$ is the local momentum at which the resonance would occur if electrons were scattered by molecules with the nuclei fixed at separation R,

$$k^2(R)/2 = E_{res}(R) - E_0(R), \tag{8}$$

with $E_0(R)$ denoting the electronic energy of the target. The barrier penetration factor is then $\gamma^{l+1/2}(k,R)$. With the introduction of this factor, the entry amplitude will be

$$\phi_\nu(r) = \gamma^{l+1/2}(k_i,R)\left(\frac{\Gamma(R)}{2\pi}\right)^{1/2}\eta_\nu(R), \tag{9}$$

The modification of Eq. (4) with Eq. (9), and the use of the same factor in the "exit amplitude" in the expression for the scattering amplitude below, constitutes the local complex potential model with barrier penetration factors.

Nonlocal model — To go beyond these simple local models, we must make use of the well-established formulation of nonlocal versions of these theories. A detailed exposition of the nonlocal theory based on the projection-operator formalism has been given by Domcke [29], and numerous references to earlier work on nonlocal potential theory can be found therein. However, in our case we are starting our calculations of the nuclear dynamics with somewhat more information than those theories ordinarily employ as their point of departure. Typically one begins with a real-valued and square-integrable approximation to the electronic resonance wave function, $\psi_{res}(\mathbf{r},R)$, where $\mathbf{r}$ denotes all the electronic coordinates. The expectation value of the $(N+1)$-electron Hamiltonian with respect to ψ_{res} gives a real-valued approximation to the resonance energy. The interaction of ψ_{res} with the continuum produces both a real-valued "shift" and a correction that gives the imaginary part of the resonance energy, or width of the resonance. In the general nonlocal theory both of these corrections appear as nonlocal and energy-dependent potentials.

Our case is different, because we have already computed the energy and width of the resonance in a complete electron-molecule scattering calculation. We have therefore calculated the real part of the resonance energy itself, and no shift correction is required. However, following the ideas of Hazi *et al.* [24] it is still possible to construct a nonlocal width function which goes correctly to the local width $\Gamma(R)$ in the limit of high energies, and that can at least partly repair some of the deficiencies of the local model.

In our nonlocal potential model we begin with Eq. (4) with the modification of the driving term given in Eq. (9). We then introduce a complex, energy-dependent, nonlocal potential, V_{res} , defined as

$$V_{res}(R,R') = E_{res}(R)\delta(R-R') \\ -i\pi\sum_{\nu}^{open} U_\nu(k_\nu,R)U_\nu(k_\nu,R'). \tag{10}$$

E_{res} is the real part of the potential energy curve of the negative ion from electron-molecule scattering calculations (or bound-state calculations in its bound region), and k_ν is the momentum of the scattering electron when the molecule is left in the final vibrational state η_ν. The sum runs over the energetically open vibrational states of the ion.

Following Hazi *et al.* [24, 30] we approximate $U_\nu(k_\nu,R)$, the matrix element coupling the resonance to the non-resonant background associated with a vibrational level ν, as

$$U_\nu(k_\nu,R) = \gamma^{l+1/2}(k_\nu,R)\left(\frac{\Gamma(R)}{2\pi}\right)^{1/2}\eta_\nu(R) \tag{11}$$

At sufficiently high incident energy one can make use of Eq. (7) and also assume that the sum over vibrational states in Eq. (10) is complete to show that in the high-energy limit the nonlocal potential in Eq. (10) produces the local width function.

$$\sum_{\nu}^{open} U_\nu(k_\nu,R)U_\nu(k_\nu,R') = \frac{\Gamma(R)}{2\pi}. \tag{12}$$

Therefore the nonlocal potential model we use here goes to the local complex potential approach, with the barrier penetration factor still present in the entry and exit amplitudes, in the limit of high energies. This nonlocal model should at least partially repair the deficiencies of the local complex potential approach when it breaks down in the case that the nuclear motion of the metastable anion takes place near a crossing of the anion and the neutral potential curves [24–26].

Amplitudes and cross sections – The resonant T-matrix for vibrational excitation or elastic scattering is obtained by projecting the solution of Eq. (4) in any of these three models onto the "exit amplitude", $\phi_{\nu'}$, given by Eq. (6) or Eq. (9) depending on the model,

$$T_{\nu\nu'}(E) = \langle\phi_{\nu'}|\xi_\nu\rangle. \tag{13}$$

Integral vibrational excitation cross sections are then given by

$$\sigma_{\nu\to\nu'} = \frac{4\pi^3}{k_i^2} \left| T_{\nu\nu'}(E) \right|^2 . \tag{14}$$

Vibrational excitation and elastic cross sections calculated for each resonance state from Eq. (14) must be multiplied by their appropriate statistical weight and added in order to be compared with experimental measurements. For the case of NO, the physical cross sections are given by

$$\sigma_{\nu\to f}^{total} = \frac{1}{8}\left(3\sigma_{\nu\to f}^{^3\Sigma^-} + 2\sigma_{\nu\to f}^{^1\Delta} + \sigma_{\nu\to f}^{^1\Sigma^+} \right). \tag{15}$$

In the case of dissociative attachment, a solution of Eq. (4) must be constructed that is regular at the origin and subject to purely outgoing boundary conditions. The integrated cross section for dissociative electron attachment from vibrational state ν is then expressed as

$$\sigma_{\nu\to DA} = g\frac{2\pi^2}{k_\nu^2}\frac{K}{\mu} \lim_{R\to\infty} |\xi_\nu(R)|^2 \tag{16}$$

where g is the ratio of resonance state to initial state statistical weights (i.e. 3/8 for the case of the $^3\Sigma^-$ resonance) and $K^2/2\mu$ is the asymptotic kinetic energy of the dissociated fragments with reduced mass μ, i.e.,

$$K^2/2\mu = E - V_{res}(R)|_{R\to\infty}. \tag{17}$$

An alternative approach to calculating dissociative attachment cross section, which we will use when interpreting the results of our calculations of this process in NO, can be derived by employing the principle of detailed balance [31], which relates the T-matrix for dissociative attachment to the T-matrix for its reverse process, associative detachment,

$$T_{\nu\to DA} = T^*_{AD\to\nu}. \tag{18}$$

This equation leads to the following relation between the cross sections,

$$m_e E_e \sigma_{\nu\to DA}(E_e) = \mu E \sigma_{AD\to\nu}(E) \tag{19}$$

where m_e, the mass of the electron, has been written explicitly for clarity, but is otherwise expressed in atomic units in this discussion. E is the total energy of the system,

$$E = E_\nu + E_e, \tag{20}$$

where E_ν is the energy of vibrational state ν and E_e is the energy of the incident electron.

From these considerations (or from an explicit examination of the asymptotic form of $\xi(R)$ in terms of the Green's function for the Hamiltonian in Eq. (4)), the cross section for dissociative attachment can be written as

$$\sigma_{\nu\to DA}(E_e) = g\frac{4\pi^2}{E_e}\frac{\mu}{K}|\langle\psi_E|\phi_\nu\rangle|^2 \tag{21}$$

where the scattering solution, ψ_E, satisfies the Schrödinger equation

$$(E - K_R - V_{res})\psi_E = 0. \tag{22}$$

The proper normalization of ψ_E will be discussed below.

Finally, we note that from these considerations it can be seen that cross sections for associative detachment to form NO are much smaller than the corresponding dissociative attachment cross sections. This point is easily deduced from Eq. (19), where the value of the reduced mass of NO ($\mu = 13614$) will imply that $\sigma_{AD\to\nu}$ is approximately 4 orders of magnitude smaller than $\sigma_{\nu\to DA}$.

B. Numerical solution of the Schrödinger equation

In order to solve the equations that govern the electron-molecule collision processes that are relevant to this study, we have made use of a finite-element method, implemented using a discrete variable representation (DVR) [32]. In the case of dissociative attachment, the generalization of this method to use exterior complex scaling (ECS) gives the additional advantage of avoiding the need for explicit imposition of asymptotic boundary conditions. Details of this very efficient numerical representation, as well as important previous developments of the DVR method, can be found in the work of Rescigno and McCurdy [32], the recent review of McCurdy *et al.* [33], and the references therein. Here we only mention some of its main features and how they relate to the present study.

A great advantage of the DVR approach is that any local operator, like the potential in the local potential model has a diagonal representation. In this approach the kinetic energy is non diagonal, but its matrix elements have simple analytic forms. Although our nonlocal potential will be non diagonal in the DVR, its matrix elements can be trivially constructed in terms of the factors $U_\nu(k_\nu, R)$ in Eq. (11) evaluated at points, R, on the DVR grid. Thus the nonlocal potential model is no more difficult to implement using the finite element DVR approach than the local potential case.

Both of the processes that are investigated here can be represented by Eq. (4). In the case of vibrational excitation, the solution $\xi_\nu(R)$ will be square integrable, and the finite element DVR approach using real-valued coordinates will constitute an adequate approach to solving Eq. (4). Dissociative electron attachment, on the other hand, requires a solution of Eq. (4) that behaves outside the interaction region as a purely outgoing wave. Exterior complex scaling allows one to easily construct such a solution without detailed consideration of asymptotic boundary conditions. The origins of this complex coordinate scaling have been discussed extensively in the recent review by McCurdy *et al.* [33]. The ECS transformation which we apply to Eq. (4) is given by

$$R \to T(R) \equiv \begin{cases} R & R < R_0 \\ R_0 + (R - R_0)e^{i\eta} & R \geq R_0 \end{cases} \tag{23}$$

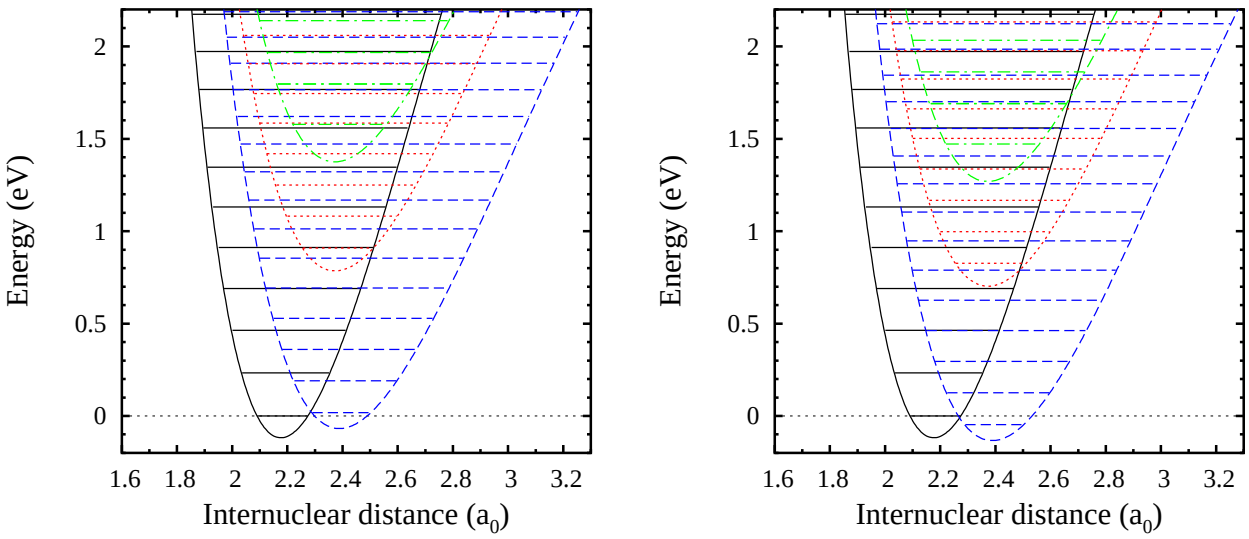

FIG. 1: (Color online) NO and NO^- potential curves and vibrational levels. Solid curves: $^2\Pi$ neutral ground-state; dashed curves: $^3\Sigma^-$ anion; dotted curves: $^1\Delta$ anion; dash-dot curves: $^1\Sigma^+$ anion. Left panel: curves obtained from configuration-interaction calculations; right panel: shifted CI curves (see text). Internuclear distances are given in atomic units, where $a_o = 5.2917721 \times 10^{-11}$ m is the Bohr radius. Energies are in units of eV = 1.6021765 $\times 10^{-19}$ J.

where R is the internuclear distance, while R_0 and η are fixed parameters of the transformation. The transformed Schrödinger equation is then solved on a grid that extends beyond R_0, into the region in which the outgoing wave falls off exponentially. The combined finite-element DVR technique offers a practical and accurate method for implementing the ECS transformation. We refer the interested reader to ref. [33] for further details. Making the radius R_0 large enough to enclose the entire interaction region allows the collision dynamics to be extracted from the region inside that radius, where coordinates are real. This transformation, as mentioned above, eliminates the need for explicit enforcement of asymptotic boundary conditions and produces a solution with the correct boundary conditions automatically.

To construct the wave function corresponding to associative detachment we must solve Eq. (22). To do so using the ECS transformation, we first write the radial scattering solution as the sum of a free function ψ_0 and a scattering wave, ψ_{sc},

$$\psi_E = \psi_0 + \psi_{sc}. \tag{24}$$

With the cross section defined by Eq. (21), ψ_0 is just $\sin(KR)$. Thus, the driven Schrödinger equation becomes

$$(E - K_R - V_{res})\psi_{sc} = V_{res}\psi_0 \tag{25}$$

which has the same form as Eq. (4) and can be solved in the same way.

C. Fixed-nuclei resonance curves

Zhang *et al.* [12] carried out fixed-nuclei scattering calculations using the complex Kohn variational method and extracted resonance energies and lifetimes for the negative ion states from Breit-Wigner fits of the relevant eigenphase sums. The trial wave functions in their calculations were constructed using modest CI expansions. The molecular orbitals were obtained by averaging the density matrices of the target and resonance states in order to strike a balance between correlation effects in the neutral and anion states. The resonance widths from that earlier study were also employed in the present calculations.

Since the quasi-bound vibrational levels of the NO^- states overlap, the electron-NO cross sections below 2 eV are highly structured. To meaningfully compare calculated cross sections with measured values requires that the relative positions of the anion states with respect to the target states be known with an accuracy of less than 0.1 eV. Practical considerations make it difficult to achieve such accuracy in scattering calculations, even with fairly elaborate trial wave functions. Electronic structure calculations were therefore carried out to better position the negative ion and target potential curves. Zhang *et al.* had previously employed coupled-cluster, single- and double-excitation calculations with a non-iterative triples correction (CCSD(T)). In the present work, we used large-scale configuration-interaction methods. CC calculations are size-consistent and are generally accurate in calculating energy differences between

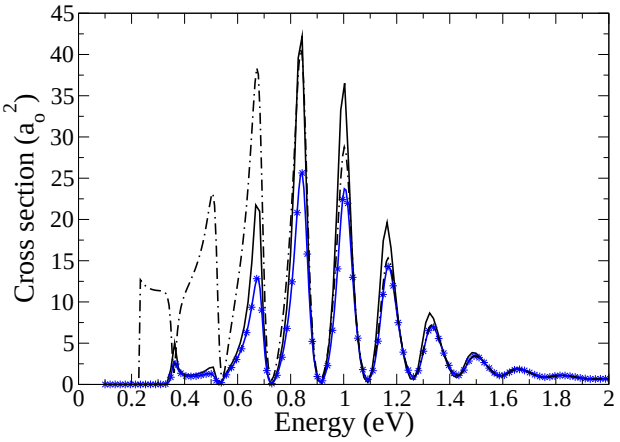

FIG. 2: (Color online) $^3\Sigma^-$ symmetry component of the e^--NO $\nu = 0 \rightarrow 1$ vibrational excitation cross section. Comparison of different theoretical models for treating the nuclear dynamics. Solid curve: nonlocal model; solid curve with stars: local complex potential model with inclusion of barrier penetration factors; dash-dot: local complex potential (boomerang) model. Cross sections are given in atomic units ($a_o^2 = 2.8002852 \times 10^{-21}$ m^2) and energies are in units of eV.

the lowest states of systems with different numbers of electrons, as in the case of NO and NO^-. On the other hand, multi-reference configuration-interaction (MRCI) calculations will give accurate results for the relative energies of the different resonance states, providing in this way, better potential curves for the calculation of dissociative electron attachment cross sections.

III. CALCULATIONS AND RESULTS

For the present study, multi-reference single- and double-excitation calculations (MRCISD) [34] were performed on the NO ground state and the $^3\Sigma^-$, $^1\Delta$ and $^1\Sigma^+$ anion states using one-electron orbitals generated from multi-reference self-consistent field (MCSCF) calculations for each state. The active space for the MCSCF calculations, as well as the reference space for the CI calculations, consisted of all the orbitals of the 2p shells of O and N, with the valence electrons distributed in all possible ways. The neutral and anion potential curves obtained from these CI calculations are shown in the left panel of Fig. 1. For all the states, the relative shapes of the curves and their equilibrium internulear distances agree with the earlier CC values. The potential curves for the neutral ground-state and the $^3\Sigma^-$ anion state are very close to the CC values previously obtained by Zhang *et al.* (cf. Fig. 6 of ref. [12]), whereas the $^1\Delta$ and $^1\Sigma^+$ anion curves lie below the previous curves by ~ 0.24 and 0.26 eV, respectively. These new results give a $^1\Delta$ curve that is in better agreement with the semi-empirical result obtained by Teillet-Billy and F. Fiquet-Fayard [21], while the new results for the $^1\Sigma^+$ state are consistent with experimental findings of Randell *et al.* [6].

The left panel of Fig. 1 illustrates the calculated neutral and anion potential curves, together with the real parts of the vibrational levels associated with each curve. For the anion states, both the real and imaginary parts of each resonance, the latter obtained from the earlier complex Kohn calculations, were used in computing the vibrational levels. While the present potential curves give results in better agreement with measured values than the earlier CC results of Zhang *et al.*, a final small adjustment of the resonance curves was carried out to better compare the theoretical cross sections with experiment. The $^3\Sigma^-$ curve was lowered by 65 meV, which brings the first three peaks in the calculated elastic cross section into good agreement with the positions of the corresponding peaks in Allan's recent high resolution measurements [9, 13]. The $^1\Delta$ curve was lowered by 83 meV, based again on Allan's high resolution elastic cross sections as further explained below. Finally, the $^1\Sigma^+$ was lowered by ~ 0.15 eV so that its asymptotic value at large internuclear distance coincided with that of the $^1\Delta$ state. The shifted curves, which were used in all the calculations described below, are shown in the right panel of Fig. 1. It is worth noting that in their semi-empirical analysis of Tronc *et al.*'s data, Teillet-Billy and F. Fiquet-Fayard assumed a coincidence of the $^3\Sigma^-(\nu = 7)$ and $^1\Delta(\nu = 2)$ levels as a criterion to position the $^1\Delta$ curve. Such a criterion, however, is invalidated by the fact that there are significant shifts, which change with the observed exit vibrational level, between the actual peak positions in the cross sections and their expected positions based on the vibrational energy level values. These shifts arise as a consequence of the finite lifetimes of the anion states against autodetachment.

A. Elastic scattering and vibrational excitation

Figure 2 shows the $\nu = 0 \rightarrow 1$ vibrational excitation cross sections calculated using three different models for treating the nuclear dynamics described in section II A: (1) the local complex potential model, as used by Zhang *et al.* in their earlier calculations, (2) the local complex potential model with barrier penetration factors included in the entry and exit amplitudes and, (3) the nonlocal model. For clarity, only the $^3\Sigma^-$ contribution to the cross section is shown. As expected, the cross sections computed without inclusion of barrier penetration factors are qualitatively incorrect at low energy and significantly overestimate the first few peaks near threshold. This behavior becomes even more pronounced in the higher excitation cross sections (not shown). The introduction of barrier penetration factors, both in the local and nonlocal approximations, produces the correct behavior of the cross sections at threshold. The latter two models produce similar results, with the nonlocal model giving slightly larger peak values in the cross sections at low energy. As the energy increases, and more vibrational

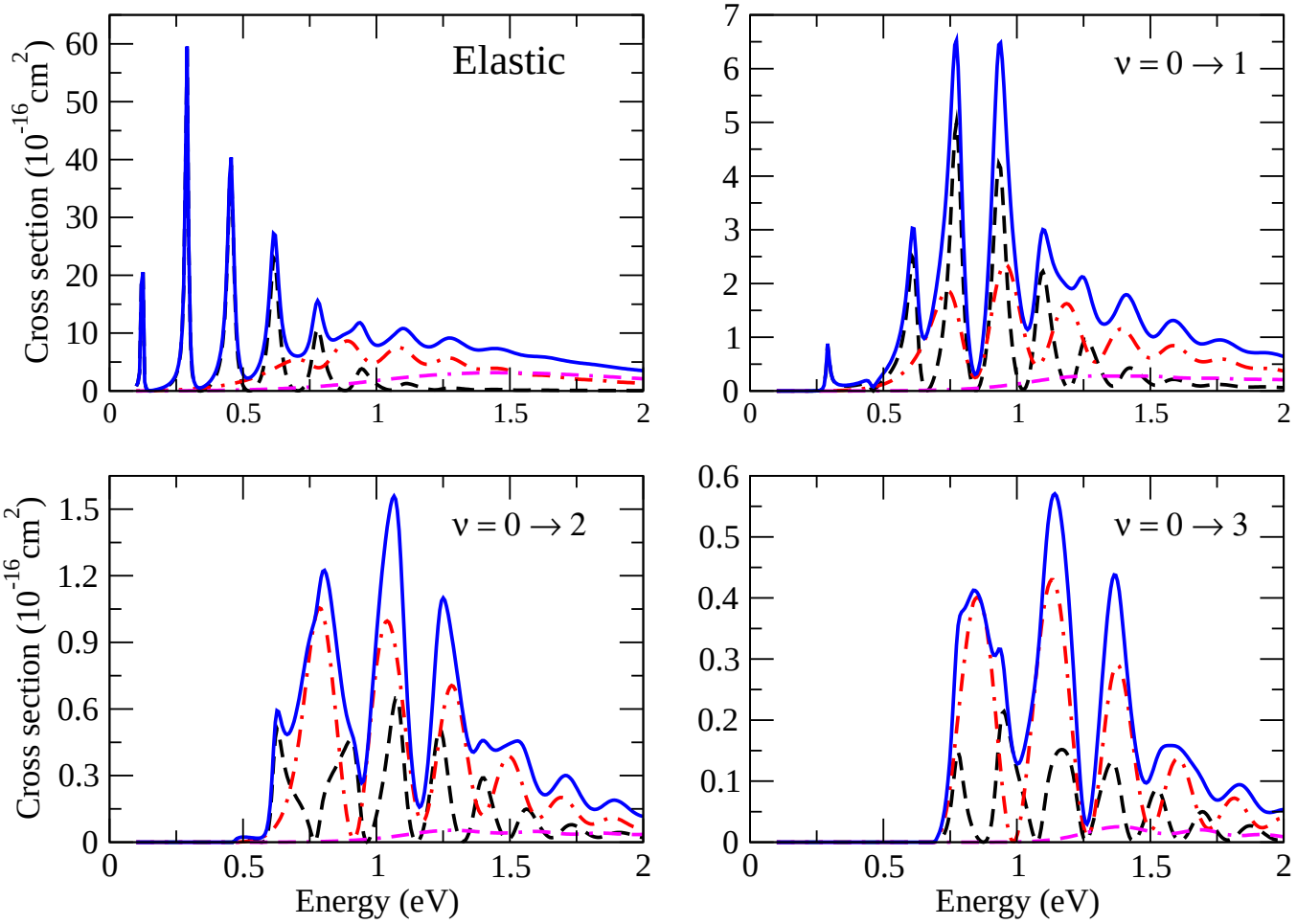

FIG. 3: (Color online) Contribution of individual resonances to the elastic and vibrationally inelastic cross sections. Solid curves: total cross sections; dashed curves: $^3\Sigma^-$ symmetry contributions; dash-dot curves: $^1\Delta$ symmetry contributions; double dash-dot curves: $^1\Sigma^+$ symmetry contributions. Individual symmetry contributions include statistical weights given in Eq. (15).

states become energetically available, all three approximations yield the same cross sections, as expected. These trends were also seen in the higher excitation cross sections. These results serve to quantify the breakdown of the simple local complex potential model in the present case where the vibrational levels of the $^3\Sigma^-$ anion are energetically close to those of the neutral target, which invalidates several key assumptions used in deriving the local complex potential model [24, 26]. All subsequent results we will present, for both vibrational excitation and dissociative electron attachment, were obtained using the nonlocal potential model.

Figure 3 shows the individual resonance contributions to the elastic and $\nu = 0 \rightarrow 1, 2, 3$ vibrationally inelastic cross sections obtained with the nonlocal model and the shifted CI potential curves described above. The $^3\Sigma^-$ and $^1\Delta$ cross sections both show pronounced boomerang structure while the $^1\Sigma^+$ resonance gives only a broad, structureless contribution to the cross sections. The $^3\Sigma^-$ peaks are narrower than the $^1\Delta$ peaks, reflecting the longer autodetachment lifetime (inverse width) of the $^3\Sigma^-$ negative ion state. The $^3\Sigma^-$ and $^1\Delta$ resonance peaks overlap strongly above .75 eV, which results in total vibrational excitation cross sections with pronounced irregularities. The basic structure of these cross sections, as Zhang *et al.* have pointed out, are readily explained by examination of the neutral and anion potential curves and vibrational levels (Fig. 1). Below 0.5 eV, the $^1\Delta$ resonance cannot be excited; the three lowest peaks in the elastic cross section arise solely from the $^3\Sigma^-$ state. This fact allowed us to fix the relative positions of the neutral and $^3\Sigma^-$ states by comparing the positions of the calculated and measured elastic peaks. In the case of the $^1\Delta$ resonance, the second peak in the $^1\Delta$ elastic cross section does not overlap any $^3\Sigma^-$ peaks and was therefore used to position the $^1\Delta$ resonance curve, as explained above. Note that the lowest $^3\Sigma^-$ vibrational state is bound and lies outside the Franck-Condon region of the neutral ground level. The first peak in the elastic cross section arises from the $\nu = 1$ level of the $^3\Sigma^-$ anion.

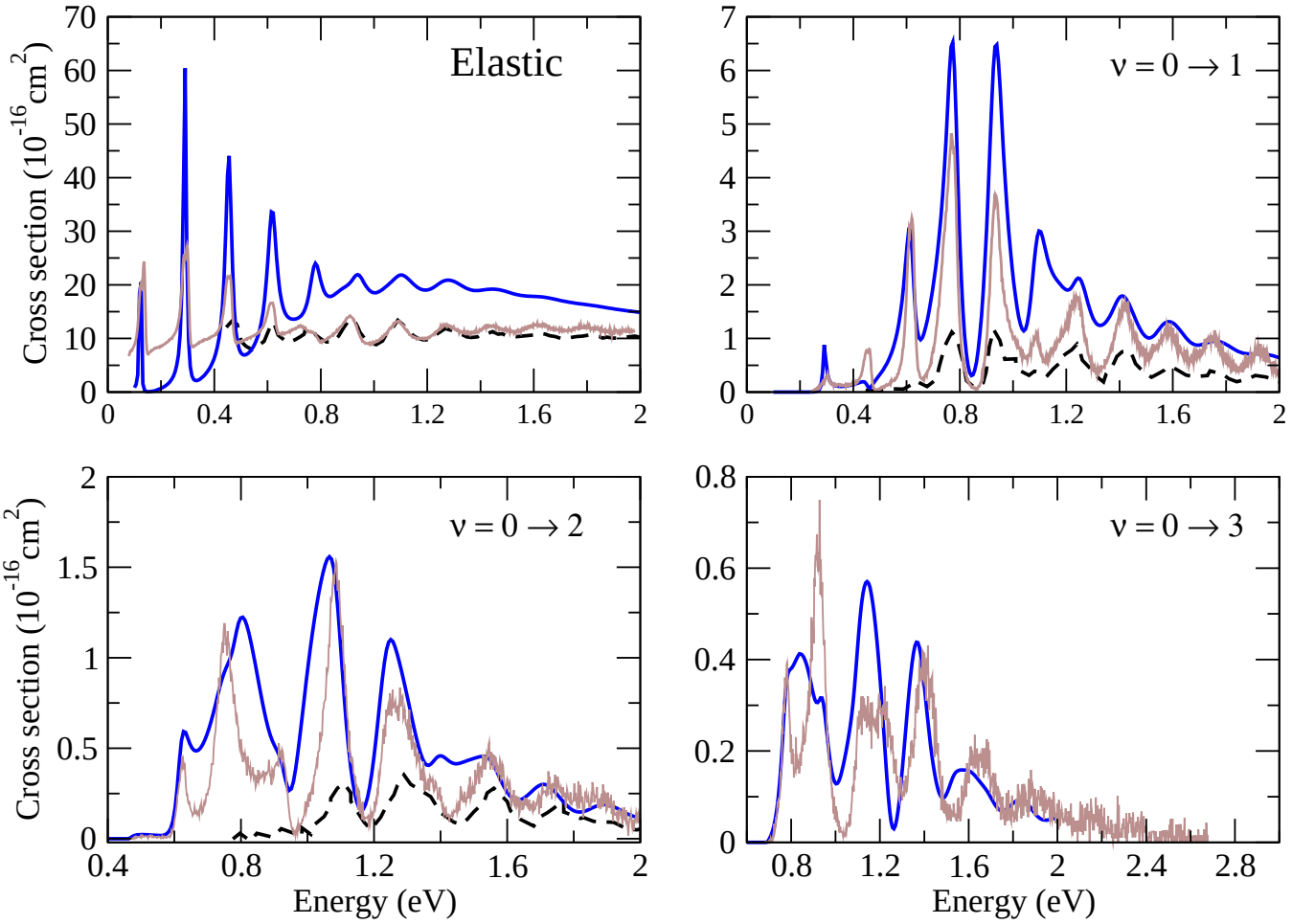

FIG. 4: (Color online) Comparison of theory and experiment for elastic and vibrationally excited cross sections. Solid dark curves: present results; dashed curves: experimental measurements of Jelisavcic *et al.* [8]; solid grey curves: experimental measurements of Allan × 4π [13].

A striking point to note about these cross sections is the fact that the peaks arising from the $^3\Sigma^-$ anion occur at energies close to the difference between the neutral and anion vibrational levels and appear at roughly the same energy in different exit channels. By contrast, the $^1\Delta$ peaks in the elastic cross section appear at energies below the anion vibrational energy levels and shift to higher energy as the excitation level increases. This behavior is caused by the shorter lifetime of the $^1\Delta$ state.

Figure 4 compares our calculated elastic and vibrationally inelastic cross sections with the recent experimental measurements of Jelisavcic *et al.* [8] and Allan [13]. All data shown is on an absolute scale with no internormalization. Jelisavcic *et al.* obtained integrated cross sections from their angular differential measurements by using a multiparameter phase shift analysis to extrapolate their cross sections to forward and backward angles. Allan made differential measurements at high resolution and was able to measure cross sections for individual fine structure levels of the target molecule. To compare with our calculations, which do not treat spin-orbit effects, and with the lower resolution measurements of Jelisavcic *et al.* , we have plotted Allan's cross sections summed over all $\Delta\Omega$ (spin-orbit) transitions.

Allan took absolute measurements at a single angle (135°), and in Fig. 4 his results were simply multiplied by 4π for this comparison. To see why this is a reasonable approximation to the integral cross section, it is instructive to consider the angular dependence of the *resonant* contribution to vibrational excitation cross section. Since the ground state of NO is doubly degenerate, we can write the electronically elastic T-matrix (for a particular vibrational transition) in the following schematic notation:

$$\mathbf{T} = \begin{pmatrix} T^{-1,-1} & T^{-1,+1} \\ T^{+1,-1} & T^{+1,+1} \end{pmatrix}, \tag{26}$$

where the superscripts on the matrices $T^{M',M}$ denote initial and final channels labeled by the M_z quantum numbers of the target. Each of these blocks is itself a square

matrix whose dimension is determined by the number of partial waves, labeled by (l, m), used to expand the fixed-nuclei wave function. The differential cross section associated with a particular transition is then

$$\frac{d\sigma^{M',M}}{d\Omega} = \sum_{l,l'} \frac{(2\pi)^4}{k_i^2} \frac{1}{8\pi^2} \times \int |Y^{\rm mol}_{l,m'}(\mathbf{k}')^* T^{M',M}_{l'm',lm} Y^{\rm mol}_{l,m}(\mathbf{k})|^2 d\omega \quad (27)$$

where the spherical harmonics refer to the body frame of the target and the integration over ω is the average over molecular orientations.

In the simplest model, we assume that for all three resonances the electron is scattered in a p-wave ($l = l' = 1$) with $m_z = \pm 1$. Which m_z component of the incident or scattered electron to associate with which target channel depends on which of the three resonances is in question. With these assumptions, the angular dependence of the cross sections can be obtained in closed form. We can now follow the logic of Dube and Herzenberg [23] to perform the necessary transformation to the lab frame and integrate over molecular orientations. The result is

$$\frac{d\sigma^{M',M}}{d\Omega} = \frac{2\pi^2}{k_i^2} |T^{M',M}|^2 \frac{3}{40} (7 + \cos(2\theta)) \quad (28)$$

and has the same form for all four possible choices of M' and M in Eq. (26) and for all three resonances . When Eq. (28) is integrated over the scattering angles, θ and ϕ, it reproduces Eq. (14).

Based on this analysis, all three resonance contributions to the integral cross section are expected to have a fairly flat angular distribution determined by the factor $7 + \cos(2\theta)$. An alternative treatment, that does not assume a single partial wave for the scattered electron, was carried out using the computed T-matrix elements (at the equilibrium internuclear distance) from the complex Kohn scattering calculations computed exactly on resonance and evaluating Eq. (27) numerically. Such a calculation gives angular dependences for the $^3\Sigma^-$ and $^1\Delta$ cross sections that are slightly different, but again nearly isotropic, as can be seen in Fig. 5. In any case, fixing θ to be 135^0, and multiplying the differential cross section by 4π gives Eq. (14) to within a few percent, so this approximate conversion of Allan's data to give integrated cross sections should be reasonable.

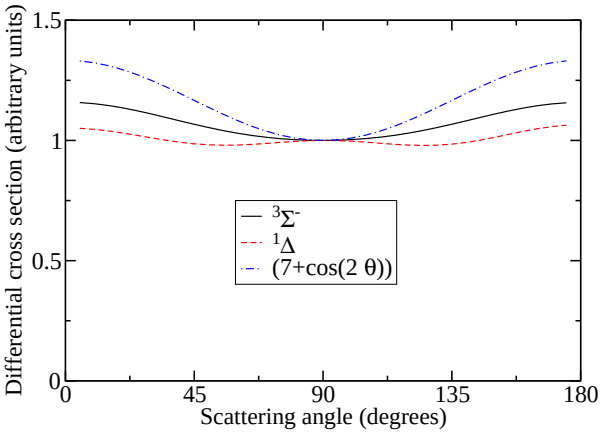

FIG. 5: (Color online) Angular dependence of resonant cross sections. With the assumption of a single partial wave, the resulting distribution is $(7 + \cos 2\Theta)$ for both $^3\Sigma^-$ and $^1\Delta$ cross sections. The angular distributions for $^3\Sigma^-$ and $^1\Delta$ are different when more partial waves are used in the analysis (see text).

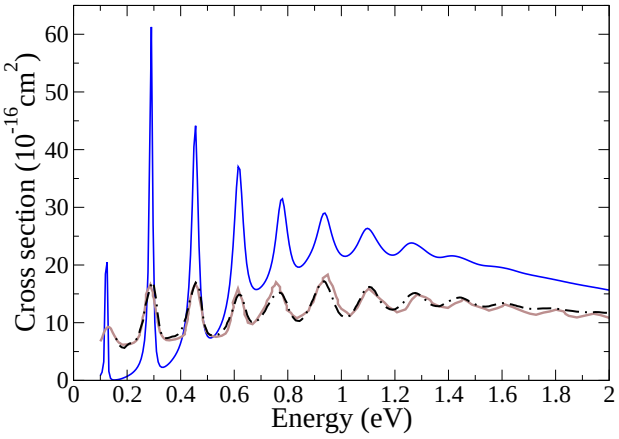

FIG. 6: (Color online) Comparison of theory and experiment for grand total cross sections. Solid dark curve: present results; dash-dot curve: experimental measurements of Alle *et al.* [5]; solid grey curve: experimental measurements of Zecca *et al.* [35].

The calculated elastic cross sections shown in Fig. 4 include the non-resonant background contributions from $^{1,3}\Pi$ symmetry calculated by Zhang *et al.* [12]. In the case of elastic scattering, there is excellent agreement bewteen the two sets of measurements above 0.8 eV, whereas the peak cross sections values near 0.45 eV and 0.6 eV measured by Allan [9, 13] are relatively larger than those measured by Jelisavcic *et al.* [8]. The agreement with theory is also rather good, the principal difference being a somewhat larger value for the background cross section given by theory. The calculated elastic cross sections show little structure above 1.5 eV, while Allan's measurements show weak structure out to 2.0 eV. Both Allan and Randell *et al.* [6] have suggested that the $^1\Sigma^+$ resonance may be responsible for structure above 1.5 eV, but our calculations predict the width of this state to be too large to give any boomerang structure.

The vibrational excitation cross sections have irregular structures, which is the result of overlapping contributions from the different resonance states. While the two sets of measured values are in reasonable agreement above 1.5 eV, they show noticeable differences at lower energies. The most striking difference is that the lowest few peaks in the $\nu = 0 \rightarrow 1$ and $\nu = 0 \rightarrow 2$ cross

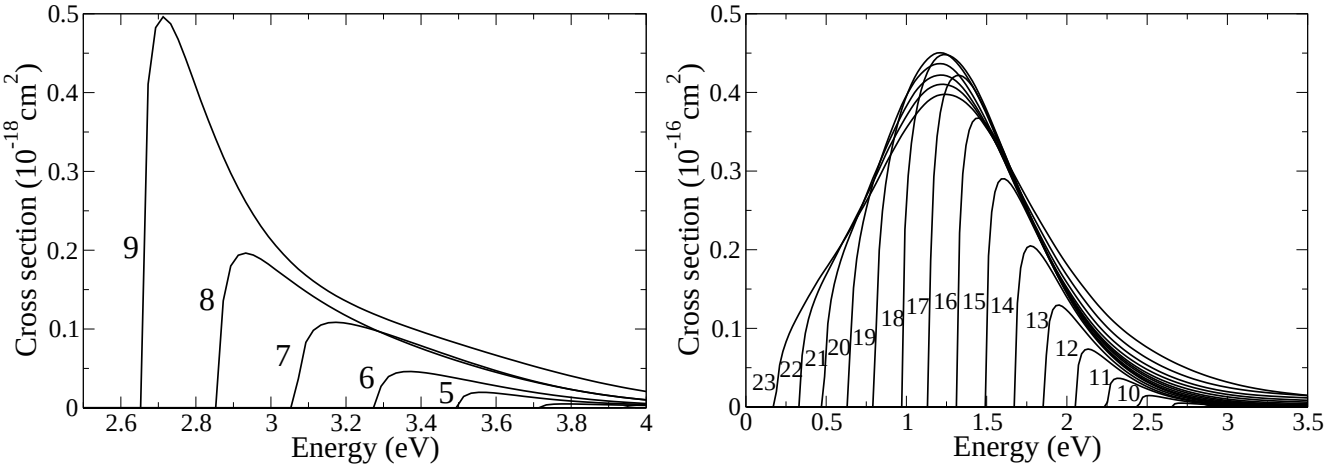

FIG. 7: Dissociative electron attachment cross sections. Left panel: cross sections from vibrationally excited states 5 through 9. Right panel: cross sections from vibrationally excited states 9 through 23.

sections, while prominent in both Allan's measurements and in our calculations as well, are strongly suppressed in the Jelisavcic *et al.* measurements. The magnitude of our calculated cross sections overall appears to be in better agreement with Allan's measurements, but we must again empasize that Allan's differential cross sections at a single angle were multiplied by 4π. The agreement between theory and experiment for the $\nu = 0 \rightarrow 3$ cross section is excellent.

The principal discrepancy between theory and experiment, which is most apparent in the case of the $\nu = 0 \rightarrow 2$ cross section, is the fact that the calculated $^1\Delta$ peaks are too broad. For example, the broad $^1\Delta$ peak at 0.8 eV in the calculated $\nu = 0 \rightarrow 2$ cross section obscures the $^3\Sigma^-$ peaks near 0.65 and 0.9 eV that are clearly seen in Allan's measurements. The calculated error in the $^1\Delta$ peaks is undoubtedly caused by an overestimate of the electronic resonance width of the $^1\Delta$ anion. The resonance widths came from earlier [12] fixed-nuclei scattering calculations, while the resonance energies came from accurate CI calculations and were further adjusted as described above. For the $^3\Sigma^-$ state, the scattering calculations and the CI calculations gave very similar resonance curves. In the case of the $^1\Delta$ state, our shifted anion curve lies $\sim$0.3 eV below the scattering results. We would expect the electronic width of the $^1\Delta$ state to therefore be smaller than the results given by our fixed-nuclei scattereing calculations. Despite some qualitative differences bewteen theory and experiment, it is clear that the overall features are properly displayed by these calculations and that the nonlocal model gives a good description of the vibrational excitation dynamics in this system.

Figure 6 shows our calculated grand total cross sections (the sum of the integrated elastic and the vibrationally inelastic cross sections) and the experimental measurements of Alle *et al.* [5], obtained by high resolution time-of-flight spectroscopy, and of Zecca *et al.* [35], who analyzed previous experimental measurements ([3, 36]). For reference, our grand total cross sections for selected energies are also tabulated in Table I. The authors will provide tabulated values for other cross sections upon request. As can be seen in Fig. 3, the most significant contribution to the grand total cross section derives from the elastic cross section, with vibrational excitation cross sections making a smaller contribution. With the exception of a slight overestimate of the nonresonant background, our calculated cross sections provide a good description of the elastic cross sections and, hence, of the grand total cross sections.

B. Dissociative electron attachment

The process of dissociative electron attachment to NO studied in the present investigation takes place via the reaction channel $e + \mathrm{NO} \rightarrow \mathrm{O}^-(^2\mathrm{P}) + \mathrm{N}(^4\mathrm{S})$, which is associated with the $^3\Sigma^-$ resonance. Fig. 7 shows the dissociative electron attachment cross sections calculated using the nonlocal potential model as described in Sec. II A. The numerical solution of the working equations of this process was carried out using the finite-element DVR implementation of ECS, as described in Sec. II B. The two panels of Fig. 7 show that the cross sections increase by several orders of magnitude as the vibrational state from which the dissociation takes place increases. We can see from these calculations that dissociative attachment proceeding from the vibrational ground state (not visible on the scale of the figure) would lead to cross sections that are too small to be detectable. However, dissociative attachment arising from vibrationally excited states should be measurable, provided the initial vibrational level is sufficiently high. Table II lists maximum values of dissociative attachment cross sections from each vibrationally excited state and the electron energy at which this cross

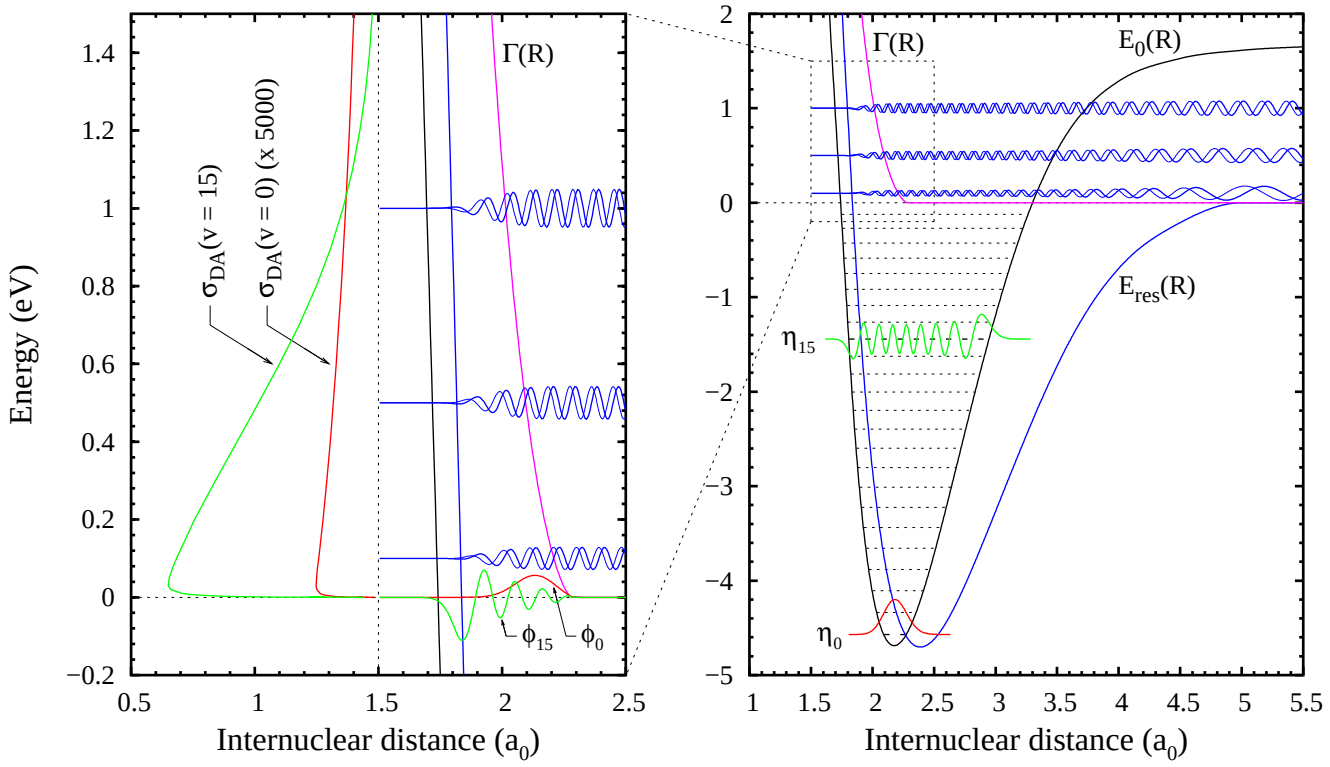

FIG. 8: (Color online) Right panel: Potential energy curves of NO and of the $^3\Sigma^-$ resonance (solid curves), and vibrational levels of the neutral target (dotted lines). Also shown are the vibrational wave functions $\eta_0(R)$ and $\eta_{15}(R)$ and the scattering solution of Eq. (22), ψ_E, at $E = 0.1$, 0.5 and 1.0 eV (solid curves). Left panel: enlargement of the selected region of the right panel. In addition to the wave functions mentioned above, the entry amplitudes $\phi_0(R)$ and $\phi_{15}(R)$ (see Eq. (6)) are shown. Vibrationally excited DA cross sections are plotted for $\nu = 0$ ($\sigma_{DA}(\nu = 0)$) $\times$ 5000, and for ν =15 ($\sigma_{DA}(\nu = 15)$). Internuclear distances are given in atomic units and energy in units of eV.

section peak is produced.

It is interesting to investigate the origin of this dramatic enhancement of the dissociative attachment cross section with vibrational excitation. The clearest way to display the physics of that enhancement is to view the process via Eq. (21) which gives the cross section in terms of the wave function, ψ_E, associated with the reverse process in which an O^- and N atom collide. The relevant wave functions and the associated potential curves are shown in Fig. 8 where it is particularly important to note the role of the imaginary part of the resonance potential curve. Vibrational wave functions of neutral NO are plotted specifically for vibrational states $\nu = 0$ and 15 in the right panel. Also shown in this panel are three scattering solutions of Eq. (22) for total energies given by Eq. (20) of $E = 0.1$, 0.5 and 1.0 eV.

A key point is that close to the classical inner turning points the scattering functions, ψ_E, appear suppressed due to the imaginary part of the resonance potential, $-i\Gamma(R)/2$. Thus there is no large peak in the scattering wave function near the classical turning point, and the enhancement of the cross section is not associated with any simple classical effect.

Evaluation of the dissociative attachment cross section using Eq. (21) requires the calculation the integral of the product of the scattering function, ψ_E, and the entry amplitude from Eq. (6), ϕ_ν. Recall that the entry amplitude is proportional to the initial vibrational wave function of the neutral multiplied by $\Gamma(R)$. The left panel of Fig. 8 is an enlargement of a selected area of the right panel that shows the entry amplitudes, $\phi_0(R)$, $\phi_{15}(R)$, associated with $\nu = 0$ and 15. Also enlarged in this panel are the scattering solutions, ψ_E. We can see that in the case of low vibrational states, the product of a rapidly oscillating scattering function, ψ_E, and a smooth vibrational wave function (e.g., $\phi_0(R)$), will give a very small overall integral. For higher vibrational states, ϕ_ν oscillates with a frequency closer to that of ψ_E, resulting in a larger integral. In this way, the cross sections for dissociative attachment are rapidly enhanced as the initial vibrational quantum number, ν, increases. The resulting cross sections for dissociation proceeding from vibrational states $\nu = 0$ multiplied by a factor of 5000 ($\sigma_{DA}(\nu = 0)$), and $\nu = 15$ ($\sigma_{DA}(\nu = 15)$), are also shown in the left panel

of Fig. 8 as a function of the total energy E.

Another noticeable characteristic of the calculated dissociative attachment cross sections is the change in their shape with the decrease of the threshold energy onset with increasing vibrational levels. This feature can be understood by taking into account the fact that the barrier penetration factor introduced in our equations will affect the cross sections only at electron energies with momenta k that are lower than the local momentum $k(R)$ in Eq. (7). As the energy of the vibrational level from which the dissociation takes place increases, the threshold energy, and thus the incident electron momentum needed for the the dissociation to occur, decreases. At $\nu \gtrsim 15$, the introduction of the barrier penetration factor gives rounded shape to dissociative attachment cross sections near threshold, whereas the cross sections from lower vibrational states are unaffected by the barrier penetration factor.

IV. DISCUSSION

We have presented electron-NO elastic and vibrational excitation cross sections for incident electron energies between 0 and 2 eV. These calculations were performed using a nonlocal potential model to describe the nuclear dynamics, together with a set of resonance potential curves that are more accurate than what we had previously employed [12]. The complex-valued potential curves were obtained by combining large-scale configuration-interaction calculations for the resonance positions with fixed-nuclei, complex Kohn calculations for determining the resonance lifetimes. The resulting low-energy scattering cross sections are dominated by shape resonance contributions associated with the $^3\Sigma^-$, $^1\Delta$ and, to a lesser extent, $^1\Sigma^+$ states of NO^- and display pronounced, overlapping boomerang structures that give irregularly shaped vibrational excitation cross sections.

The inclusion of "barrier penetration factors" in these calculations, in both the entry and exit amplitudes, enforces the correct threshold behavior in the resonant cross sections for vibrational excitation and removes the spurious threshold peaks that were seen in earlier boomerang calculations. However, in contrast to what was seen in earlier experiments [8], we do not find a complete supression of the lowest few peaks in cross sections for exciting higher vibrational levels, but instead find encouragingly good agreement with the recent experiments of Allan [9, 13].

We have also investigated dissociative electron attachment to NO via the $^3\Sigma^-$ negative ion resonance which gives ground state $N(^4S) + O^-(^2P)$. Our results show that the dissociative attachment cross sections in this channel that originate from the ground vibrational state of NO are extremely small, as confirmed by several experimental studies [17–20]. However, the dissociative attachment cross section is predicted by these calculations to increase by several orders of magnitude when the dissociation takes place from vibrational excited states of NO. We predict that dissociative attachment cross sections producing ground state atomic products should be measurable starting from vibrational levels above approximately $\nu = 10$.

Acknowledgments

Work at the University of California Lawrence Berkeley National Laboratory was performed under the auspices of the US Department of Energy under contract DE-AC03-76SF00098 and was supported by the U.S. DOE Office of Basic Energy Sciences, Division of Chemical Sciences. A.E.O. also acknowledges support from the National Science Foundation (Grant No. PHY-99-87877).

[1] D. Spence and G. J. Schulz, Phys. Rev. A **3**, 1968 (1971).
[2] P. D. Burow, Chem. Phys. Lett. **26**, 265 (1974).
[3] A. Zecca, I. Lazzizzera, M. Krauss, and C. E. Kuyatt, J. Chem. Phys. **61**, 4560 (1974).
[4] M. Tronc, A. Huetz, M. Landau, F. Pichou, and J. Reinhardt, J. Phys. B **8**, 1160 (1975).
[5] D. T. Alle, M. J. Brunger, and S. J. Buckman, J. Phys. B **29**, L277 (1996).
[6] J. Randell, S. L. Lunt, G. Mrotzek, D. Field, and J. P. Ziesel, Chem. Phys. Lett. **252**, 253 (1996).
[7] L. Josic, T. Wroblewski, Z. L. Petrovic, J. Mechlinska-Drewko, and G. P. Karwasz, Chem. Phys. Lett. **350**, 318 (2001).
[8] M. Jelisavcic, R. Panajotovic, and S. J. Buckman, Phys. Rev. Lett. **90**, 203201 (2003).
[9] M. Allan, Phys. Rev. Lett. **93**, 063201 (2004).
[10] J. Tennyson and C. J. Noble, J. Phys. B **19**, 4025 (1986).
[11] F. J. da Paixao, M. A. P. Lima, and V. McKoy, Phys. Rev. A **53**, 1400 (1996).
[12] Z. Zhang, W. Vanroose, C. W. McCurdy, A. E. Orel, and T. N. Rescigno, Phys. Rev. A **69**, 062711 (2004).
[13] M. Allan, J. Phys. B. **38**, 603 (2005).
[14] R. J. V. Brunt and L. J. Kieffer, Phys. Rev. A **10**, 1633 (1974).
[15] E. Krishnakumar and S. K. Srivastava, J. Phys. B **21**, L607 (1988).
[16] O. J. Orient and A. Chutjian, Phys. Rev. Lett. **74**, 5017 (1995).
[17] Y. Chu, G. Senn, P. Scheier, A. Stamatovic, T. D. Mark, F. Brüning, S. Matejcik, and E. Illenberger, Phys. Rev. A **57**, R697 (1998).
[18] G. Denifl, D. Muigg, A. Stamatovic, and T. D. Märk, Chem. Phys. Lett. **288**, 105 (1998).
[19] E. Illenberger and T. D. Märk, Phys. Rev. Lett. **82**, 4364 (1999).
[20] M. Allan, J. Phys. B **37**, L359 (2004).

[21] D. Teillet-Billy and F. Fiquet-Fayard, J. Phys. B **10**, L111 (1977).
[22] T. F. O'Malley, Phys. Rev. **150**, 14 (1966).
[23] L. Dube and A. Herzenberg, Phys. Rev. A **20**, 194 (1979).
[24] A. U. Hazi, T. N. Rescigno, and M. Kurilla, Phys. Rev. A **23**, 1089 (1981).
[25] R. K. Nesbet, Phys. Rev. A **19**, 551 (1979).
[26] R. J. Bieniek, J. Phys. B **13**, 4405 (1980).
[27] J. N. Bardsley, in *Electron-Molecule and Photon-Molecule Collisions*, edited by T. N. Rescigno, V. McKoy, and B. I. Schneider (Plenum, New York, 1979), p. 267.
[28] J. N. Bardsley and J. M. Wadehra, J. Chem. Phys. **78**, 7227 (1983).
[29] W. Domcke, Physics Reports **208**, 97 (1991).
[30] A. U. Hazi, A. E. Orel, and T. N. Rescigno, Phys. Rev. Lett. **46**, 918 (1981).
[31] J. R. Taylor, *Scattering Theory: The Quantum Theory of Nonrelativistic Collisions* (John Wiley & Sons, Inc., 1972).
[32] T. N. Rescigno and C. W. McCurdy, Phys. Rev. A **62**, 032706 (2000).
[33] C. W. McCurdy, M. Baertschy, and T. N. Rescigno, J. Phys. B **37**, 2004 (R137-R187).
[34] Calculations were made with MOLPRO, a quantum chemistry package of *ab initio* programs designed by H.-J. Werner and P. J. Knowles, version 2002.1, R. D. Amos, A. Bernhardsson, A. Berning, P. Celani, D. L. Cooper, M. J. O. Deegan, A. J. Dobbyn, F. Eckert, C. Hampel, G . Hetzer, P. J. Knowles, T. Korona, R. Lindh, A. W. Lloyd, S. J. McNicholas, F. R. Manby, W. Meyer, M. E. Mura, A. Nicklass, P. Palmieri, R. Pitzer, G. Rauhut, M. Schütz, U. Schumann, H. Stoll, A. J. Stone, R. Tarroni, T. Thorsteinsson, and H.-J. Werner. http://www.molpro.net/info/current//doc/molpro.bib.
[35] A. Zecca, G. P. Karawasz, R. S. Brusa, and T. Wróblewski, Int. J. Mass Spectrom. **223-224**, 205 (2003).
[36] C. Szmytkowski and K. Maciąg, J. Phys. B **24**, 4273 (1991).

TABLE I: Calculated e^--NO grand total cross sections (GTCS) as a function of energy. Cross sections are in units of 10^{-16} cm^2 and energies are in eV.

Energy	GTCS	Energy	GTCS	Energy	GTCS
0.1000	0.8320	0.7354	19.4719	1.3709	21.3185
0.1127	3.2252	0.7481	22.3429	1.3836	21.4026
0.1254	20.5018	0.7608	26.9145	1.3963	21.5218
0.1381	0.3518	0.7735	31.2134	1.4090	21.5888
0.1508	0.06775	0.7862	30.1425	1.4217	21.5626
0.1635	0.1200	0.7989	25.5610	1.4344	21.4518
0.1762	0.2485	0.8117	22.0260	1.4471	21.2770
0.1889	0.4699	0.8244	20.2311	1.4598	21.0570
0.2016	0.7435	0.8371	19.6350	1.4725	20.8099
0.2143	1.0987	0.8498	19.7636	1.4852	20.5546
0.2270	1.5948	0.8625	20.3278	1.4979	20.3148
0.2397	2.3645	0.8752	21.1866	1.5107	20.1146
0.2525	3.7583	0.8879	22.3143	1.5234	19.9703
0.2652	6.9256	0.9006	23.8366	1.5361	19.8814
0.2779	18.7501	0.9133	25.9359	1.5488	19.8261
0.2906	61.2796	0.9260	28.1865	1.5615	19.7778
0.3033	10.1580	0.9387	28.9980	1.5742	19.7195
0.3160	3.1994	0.9515	27.5446	1.5869	19.6446
0.3287	2.2709	0.9642	25.3023	1.5996	19.5518
0.3414	2.3782	0.9769	23.4854	1.6123	19.4388
0.3541	2.8238	0.9896	22.2825	1.6250	19.3062
0.3668	3.4695	1.0023	21.6604	1.6377	19.1486
0.3795	4.3272	1.0150	21.5018	1.6505	18.9713
0.3923	5.5048	1.0277	21.7097	1.6632	18.7956
0.4050	7.2673	1.0404	22.2205	1.6759	18.6307
0.4177	10.2128	1.0531	23.0255	1.6886	18.4817
0.4304	16.1795	1.0658	24.1311	1.7013	18.3470
0.4431	30.1699	1.0786	25.3802	1.7140	18.2227
0.4558	44.1474	1.0913	26.2417	1.7267	18.1037
0.4685	23.2452	1.1040	26.2254	1.7394	17.9878
0.4812	11.6303	1.1167	25.4906	1.7521	17.8734
0.4939	8.2425	1.1294	24.4993	1.7648	17.7592
0.5066	7.3877	1.1421	23.5439	1.7775	17.6435
0.5193	7.4823	1.1548	22.7453	1.7903	17.5255
0.5321	8.0750	1.1675	22.1560	1.8030	17.4033
0.5448	9.0707	1.1802	21.8044	1.8157	17.2778
0.5575	10.5562	1.1929	21.7108	1.8284	17.1513
0.5702	12.8291	1.2056	21.8847	1.8411	17.0259
0.5829	16.5922	1.2183	22.3224	1.8538	16.9032
0.5956	23.2862	1.2311	22.9361	1.8665	16.7844
0.6083	33.4398	1.2438	23.5053	1.8792	16.6692
0.6210	36.5577	1.2565	23.8026	1.8919	16.5574
0.6337	27.3836	1.2692	23.7780	1.9046	16.4486
0.6464	20.3016	1.2819	23.5242	1.9173	16.3426
0.6591	17.1405	1.2946	23.1458	1.9301	16.2385
0.6719	15.9589	1.3073	22.7151	1.9428	16.1355
0.6846	15.7470	1.3200	22.2494	1.9555	16.0327
0.6973	16.0603	1.3327	21.8407	1.9682	15.9254
0.7100	16.7254	1.3454	21.5302	1.9809	15.8159
0.7227	17.7824	1.3581	21.3518	2.0000	15.6514

TABLE II: Maximum values of calculated dissociative electron attachment cross sections (DACS) from vibrationally excited states (ν_i) of NO and energies of the incident electron at which these cross sections are produced. Cross sections are in units of 10^{-16} cm^2 and energies are in eV.

ν_i	Energy	DACS	
0		4.8548497	2.6921455×10^{-5}
1		4.5945892	7.3894421×10^{-5}
2		4.4144088	1.9972127×10^{-5}
3		4.3743687	5.0167238×10^{-5}
4		3.7737675	4.9256797×10^{-5}
5		3.5535471	1.9656159×10^{-4}
6		3.3733667	4.6051432×10^{-4}
7		3.1731663	1.0852484×10^{-3}
8		2.9329259	1.9636015×10^{-3}
9		2.7127054	4.961709×10^{-3}
10		2.5125050	1.4583266×10^{-2}
11		2.3123046	3.6489216×10^{-2}
12		2.1321242	7.3736554×10^{-2}
13		1.9519439	0.12963221
14		1.7717635	0.20493259
15		1.6116032	0.2901275
16		1.4514429	0.36741663
17		1.3313226	0.42170441
18		1.2312224	0.44816816
19		1.2112024	0.45041918
20		1.2112024	0.43657256
21		1.2112024	0.42207784
22		1.2312224	0.41033554
23		1.2312224	0.3975291